

# Microstructure evolution of Al-Si hypoeutectic alloys prepared by controlled diffusion solidification

Abbas Khalaf (✉ [abbasklf6@yahoo.com](mailto:abbasklf6@yahoo.com))

McMaster University <https://orcid.org/0000-0002-0157-8491>

---

## Research Article

**Keywords:** Controlled diffusion solidification, Al-Si alloys, microstructure, optical metallography

**Posted Date:** January 17th, 2022

**DOI:** <https://doi.org/10.21203/rs.3.rs-1255243/v1>

**License:**  This work is licensed under a Creative Commons Attribution 4.0 International License.

[Read Full License](#)

---

# Abstract

The possibility of changing the dendritic microstructure associated with the conventional casting processes of hypoeutectic Al-Si alloys to non-dendritic microstructure by using the controlled diffusion solidification process (CDS) has been investigated. The successful CDS process depends on mixing two precursor alloys heated at a superheat condition near their respective liquidus temperature. Experimental work and simulation work using Ansys software was carried out in the present study by employing Al-Si and Al-Cu systems. This study investigates the effect of the content of the two precursor alloys, the mass ratio changing from 2.6 to 8.3, and the superheat of the first precursor alloy on changing the microstructure. The experimental results show that the pure aluminum used as the first precursor alloy needs more undercooling and agitation during the mixing to form the non-dendritic microstructure compared with hypoeutectic Al-Si alloys. Further, mixing pure aluminum with hypereutectic alloy can change the microstructure of hypoeutectic alloys leading to extending the possibility to choose the second precursor alloy. The results also show that a higher mass ratio is preferred when mixing pure aluminum with hypoeutectic alloy. Furthermore, the microstructure of the alloy Al- 6.45Si- 4Cu- 0.5Mg- 0.66Fe- 0.66 wt%Zn was successfully changed via the CDS process by mixing Al- 7.75Si- 0.79Fe- 0.78Zn- 0.6 wt%Mg at 2°C superheat into Al-24 wt%Cu at around 5°C superheat. The simulation results show that lower air bubbles and better distribution of the two precursor alloys happen during the mixing step when using the Al-Cu system.

## 1 Introduction

The hypoeutectic aluminum-silicon alloys are abundant among the other alloys used in the casting process. The Al-Si alloys have wide application in domestic, automotive, and aerospace applications due to their low cost, good castability, favorable mechanical properties, and high strength to weight ratio [1–4].

The controlled diffusion solidification (CDS) process depends on mixing two precursor alloys in a liquid state innovated to enable casting of aluminum wrought alloys to near-net-shape resulting to form a non-dendritic microstructure similar to that forming in the semi-solid processes [5–10]. Khalaf [11] mixed pure aluminum into Al-Si eutectic alloy to make Al-1.8 wt%Si as a resultant alloy. The results show that the non-dendritic morphologies form the microstructure of the final solidified alloy. Khalaf et al. [6, 10–16] used the CDS process to mix pure aluminum with Al-Cu binary alloys that have different solute contents, the results show that the microstructure forms from globular morphologies, globular mixed with rosette morphologies, and rosette mixed with dendritic morphologies, where the change in the microstructure strongly depends on the mass ratio and the undercooling of the first precursor alloy. The undercooling strongly depends on the difference between the initial temperatures of the two precursor alloys prior to the mixing step [12, 17].

Ghiaasiaan et al [9, 18–21] worked on the heat treatment of 7xxx (Al-Zn-Mg-Cu) wrought alloys that were made via the CDS process. Ghiaasiaan mixed two alloys instead of mixing pure aluminum into alloy

using tilt pour gravity casting equipment that has a permanent steel mold heated to 375°C [22]. The results show that the non-dendritic morphologies form the microstructure of the resultant alloy. Yang et al.[23] used the CDS process to make 7050 alloy by mixing pure aluminum into Al-Zn11.2-Mg5- Cu3 (wt%) alloy, the non-dendritic microstructure forms the resultant alloy. Khalaf [17] used Al-Zn binary alloys to study the microstructure of the CDS process, where pure aluminum was mixed into Al-Zn binary alloys at different mass ratios to make Al-4.5 wt%Zn as a resultant alloy. The final results were compared with Al-Cu alloys. Khalaf found that the non-dendritic microstructure has globular, rosettes, and dendritic morphologies coexisting in the entire samples of different experiments, where the ratio between the morphologies depends on the mass ratio, crucible temperature, and the difference between the initial temperatures of the mixed precursor alloys.

There are few studies published regarding changing the microstructure of the hypoeutectic Al-Si alloys by using the CDS process. This work was dedicated to changing the microstructure of the hypereutectic Al-Si alloys formed via the CDS process. Experimental and simulation evidence coupled with optical microstructure images support the discussion in this study.

## 2 Experiments

Table 1 presents the list of the experiments carried out along with the independent parameters and constants. The experimental procedure, the crucible and funnel dimensions, and the schematic diagram of the setting up of the funnel and the crucible for the CDS process have been discussed in detail previously[11, 16, 17]. Fig. 1(a) shows the *Alloy1* and *Alloy2* with their temperatures and concentrations placed on the Al-Si phase diagram, where *Alloy1* is pure aluminum with  $T_1$  fixed at 665°C for the CDS experiments named *Ex1* to *Ex7* involved in Table 1. Fig. 1(b) shows the cooling curve and the first derivative curve ( $dT/dt$ ) for the pure aluminum that was used in the experiments. In Fig. 1(b), the intercept point is 660.2°C representing the melting point of the used pure aluminum.

The CDS experiments named *Ex1* and *Ex2* were carried out by mixing *Alloy1* into *Alloy2* through a 9-mm diameter funnel to make the resultant alloy (*Alloy3*). *Ex1* was carried out by mixing *Alloy1* into *Alloy2* (Al-12.6 wt%Si) with  $mr$  6 to make 1.8 wt%Si as a resultant alloy. Fig. 1(c) shows the cooling curve and the first derivative curve ( $dT/dt$ ) for the Al-12.6 wt%Si eutectic alloy that was used in the experiments. In Fig. 1(c), the intercept point is 573°C representing the liquidus temperature of the used eutectic alloy. *Ex2* was carried out by mixing *Alloy1* into *Alloy2* (Al-33 wt%Cu) with  $mr$  6 to make 4.6 wt%Cu as a resultant alloy. The temperature of the mixture of *Ex1* and *Ex2* was collected by two thermocouples named lower thermocouple and upper thermocouple inserted prior to the mixing step in the bottom and the middle of the crucible, respectively. Elaboratory discussion about mixing through a funnel was already reported [13].

The CDS experiments named *Ex3*, *Ex5*, and *Ex7* were carried out by direct mixing of *Alloy1* into *Alloy2* to make the resultant alloy (*Alloy3*). *Ex3* was carried out by mixing *Alloy1* into *Alloy2* (Al-12.6 wt%Si) with  $mr$  8.3 to make 1.4 wt%Si as a resultant alloy. After the mixing step, the mixture was directly poured into an empty-backed clay crucible heated at 570°C. *Ex4* was carried out by re-melting a part of the solidified

sample of *Ex3* and directly pouring the melt into an empty-backed clay crucible that was heated at 570°C. *Ex4* represents a conventional solidification. *Ex5* was carried out by mixing *Alloy1* into *Alloy2* (Al-12.6 wt%Si) with *mr3* to make 3.1 wt%Si as a resultant alloy. After the mixing step, the mixture was directly poured into an empty steel crucible heated at 580°C. *Ex6* was carried out by re-melting a part of the solidified sample of *Ex5* and directly pouring the melt into an empty steel crucible that was heated at 580°C. *Ex6* represents a conventional solidification. *Ex7* was carried out by mixing *Alloy1* into a hypereutectic alloy (*Alloy2* (Al-15 wt%Si)) with *mr2.6* to make 4.5 wt% Si as a resultant alloy. Fig. 1(d) shows the cooling curve and the first derivative curve (dT/dt) for the Al-15 wt%Si hypereutectic alloy that was used to make *Ex7*. In Fig. 1(d), the intercept point is 609°C representing the liquidus temperature of the Al-15wt%Si alloy used in the study.

Table 1

Experimental designations with independent parameters and constants for the laboratory experiments.

Designation	Alloy 1			Alloy 2			<i>mr</i>	Alloy3		
	m1 (g)	T <sub>1</sub> C <sub>1</sub> (°C) (wt%)	T <sub>L1</sub> (°C)	m2 (g)	T <sub>2</sub> C <sub>2</sub> (°C) (wt%)	T <sub>L2</sub> (°C)			Co (wt%)	
<i>Ex1</i>	284	665 0	660	47	582 12.6	573	6	1.8		
								Si		
<i>Ex2</i>	290	664 0	660	48	552 33	549	6	4.6		
								Cu		
<i>Ex3</i>	290	665 0	660	35	580 12.6	573	8.3	1.4		
								Si		
<i>Ex4</i>	Part of <i>Ex3</i> sample re-melted at 665°C and poured directly into hot crucible at 570C									
<i>Ex5</i>	252	665 0	660	78	580 12.6	573	3	3.1		
								Si		
<i>Ex6</i>	Part of <i>Ex5</i> sample remelted at 665°C and poured into a hot steel crucible heated at 580°C									
<i>Ex7</i>	298	665 0	660	116	613 15	609	2.6	4.5		
								Si		

*Ex8* and *Ex9* were carried out by mixing alloy with alloy, where *Alloy1* was directly mixed into *Alloy2* to make *Alloy3*. Table 2 presents the independent parameters and constants for the experiments. Fig. 1(e) shows the cooling curve and the first derivative curve (dT/dt) for the *Alloy1* that was used to make *Ex9* taken as an example. In Fig. 1(e), the intercept point is 602°C representing the liquidus temperature of the *Alloy1*. Fig. 1(f) shows half of the sample produced by the CDS process. Specimens pointed by a circle

(A) and (B) represent the middle and the edge of the sample, respectively. The specimens were prepared for optical microscope images.

Table 2  
Experimental designations with independent parameters and constants for the laboratory experiment named *Ex8* and *Ex9*.

	<i>Alloy1</i>	$T_{L1}$ (°C)	$T_1$ (°C)	<i>Alloy2</i>	$T_{L2}$ (°C)	$T_2$ (°C)	<i>mr</i>	<i>Alloy3</i>
<i>Ex8</i>	Al-5.36Cu-0.88Fe- 0.67Mg-3.9Si-0.88Zn	618	630	Al-  13.5wt%Si	585	600	3	Al-  6.45Si-4Cu- 0.5Mg-0.66Fe- 0.66Zn
<i>Ex9</i>	Al-  7.75Si-0.79Fe-0.78Zn- 0.6Mg	602	604	Al-  24wt%Cu	590	593	4.5	

### 3 Phase Diagram Consideration

Figure 2 (a) shows a comparison between the phase diagram of the hypoeutectic alloys for Al-Si and Al-Cu alloys. In Figure 2 (a),  $T_L$  and  $T_S$  were the liquidus and the solidus temperature lines, respectively. The Al-Cu system was chosen to compare with the Al-Si system because the microstructure of the Al-Cu alloys easily and successfully changes to non-dendritic by using the CDS process [6, 7, 24–27, 10–17]. Figure 2 (a) can be employed to make two resultant alloys that have the same content of 4.5 wt% taken as an example. Where points (C) and (E) represent the resultant alloys that have content of Al-4.5 wt%Cu and Al-4.5 wt%Si, respectively. Unlimited contents of *Alloy1* and *Alloy2* can be chosen to make the two alloys that could be mixed to make the resultant alloy by the CDS process. Pure aluminum with 5°C superheat represented at point (A) can be mixed with eutectic alloys that have 5°C superheat represented by points (B) and (C) for Al-Cu and Al-Si systems to make the resultant alloys, respectively. According to the phase diagram, the maximum difference in the initial temperature between the pure aluminum and the eutectic alloys was 110 and 83°C employed by Al-Cu and Al-Si systems, respectively. Where, a higher difference between the temperatures of the two precursor alloys that are mixed at a temperature near to their respective liquidus temperature leads to a higher undercooling of the first precursor alloy happening during the mixing step resulting in a drastic increase in the nucleation rate [16, 17]. In addition, according to the level rule, the mass ratios ( $mr=m1/m2$ ) required to make the resultant alloys are 6.3 and 1.82 for Al-Cu and Al-Si, respectively. One can suggest that the lower difference in the initial temperature for the Al-Si system decreases the undercooling of *Alloy1* during the mixing step, this leads to a decrease in the nucleation rate. In addition, the lower mass ratio increases the amount of the dendritic morphologies forming among the globular and rosette morphologies creating in the microstructure of the hypoeutectic alloys formed by the CDS process [12, 15–17]. According to that, the microstructure of the Al-Si hypoeutectic alloys is expected to have more dendritic morphologies forming in the entire product made by the CDS process especially for the alloys that have a silicon content of more than 4.5 wt%Si when mixing pure aluminum into a hypoeutectic alloy.

## 4 Simulation Consideration

Anslys fluent software was used to simulate the mixing of *Alloy1* into *Alloy2* for the experiments *Ex1* and *Ex2* illustrated in Table 1. The 2D axisymmetric model was employed to simulate the mixing step using heat transfer, k-ε turbulence model, and the volume of fluid (VOF) with three phases model. Where dry air, pure aluminum (*Alloy1*), and *Alloy2* (Al-12.6 wt%Si for *Ex1* and Al-33 wt%Cu for *Ex2*) were the three phases coexisting in the simulation. Eqs. (1) to (3) represent the Navier stocks equation, continuity equation, and heat equation numerically solved in the simulation. Fig. 2 (b) shows the initial condition of the density distribution and the locations of the *Alloy1*, *Alloy2*, and the Air in the funnel and the crucible.

$$\frac{\partial \mathbf{u}}{\partial t} + \rho \mathbf{u} \cdot \nabla \mathbf{u} = \nabla \cdot [ - p + \mu(\nabla \mathbf{u}) ]$$

1

$$\rho \frac{\partial \rho}{\partial t} + \rho \nabla \cdot \mathbf{u} = 0$$

2

$$\rho C_p \frac{\partial T}{\partial t} + \rho C_p \mathbf{u} \cdot \nabla T = \nabla \cdot (K \nabla T)$$

3

The parameters used in Eqs. (1) to (3) were  $\rho = 2375 \text{ (kg/m}^3\text{)}$  [13, 15] is the density of the pure aluminum (*Alloy1*) at liquidus temperature, Eq. (4) represents the density of the liquid phase for hypoeutectic Al-Si alloys extrapolated from Thermo-Calc data as a function of the temperature and silicon content (wt%). In Eq. (4),  $A_L = 2528 + 3.374 C_{Si}$ ,  $B_L = 0.23234 + (4E-5) C_{Si}$ . Eq. (5) [15] represents the density of the Al-Cu hypoeutectic alloys extrapolated from data obtained from Factsage software to cover a range of copper concentrations and temperatures from (0 to 33) wt%Cu and (549.8 to 700)°C, respectively. In Eq. (5),  $\beta_T = -4.032 + (1.654E - 2)T - (2.53E - 5)T^2 + (1.23E - 8)T^3$  and  $\beta_C = 22.19678 + (0.1629)C_{Cu} + (9.0973E - 4)C_{Cu}^2 + (2.004E - 5)C_{Cu}^3$  are variables that depend on the temperature and copper concentration, respectively. Fig. 2 (c) shows a comparison between the density of the Al-12.6 wt%Si and Al-33 wt%Cu, showing that the density of Al-Cu eutectic alloy is significantly bigger than that of Al-Si eutectic alloy. Further in Eqs. (1) to (4),  $C_p$  is the specific heat, where  $C_{P-Al} = 1179$  [28],  $C_{P-Al-33Cu} = 953.9 \text{ J kg}^{-1} \text{ K}^{-1}$  [12],  $C_{P-Al-12.6Si} = 1106 \text{ J kg}^{-1} \text{ K}^{-1}$  was extrapolated in the same way for Al-Cu system [12].  $K_L = 70$  [29] and  $K_L = 95 \text{ W m}^{-1} \text{ k}^{-1}$  [30] for Al-Si and Al-Cu system respectively.  $\mu = 1.3 \text{ mPa}$  [28] is the viscosity of pure aluminum at the melting temperature ( $T_m$ ), and Eq. (6) [31] evaluates the viscosity ( $\eta_{Alloy}$ ) of a multi-component alloy that has (N) species. In Eq. (6),  $x_i$ ,  $\eta_i^0$  and  $E_i$  were alloy content in mole fraction, pre-exponential parameter, and the activation energy for pure melts, where  $\eta_{Al}^0 = 0.163 \text{ mPa} \cdot \text{s}$ ,  $\eta_{Si}^0 = 0.107 \text{ mPa} \cdot \text{s}$ ,  $\eta_{Cu}^0 = 0.398 \text{ mPa} \cdot \text{s}$ ,  $E_{Al} = 16114$

J.mole<sup>-1</sup>, E<sub>Si</sub>=23488 J.mole<sup>-1</sup>, and E<sub>Cu</sub>=25996 J.mole<sup>-1</sup> [32]. Further in Eq(6), ΔH<sub>sol</sub> is the heat of solution evaluated in Eq. (7). Where the solute content was in the mole fraction, Ω is the regular solution parameter evaluated in Eq. (8) [33]. In Eq. (8) L<sup>0</sup><sub>Al-Si</sub>= -11340-1.234T, L<sup>1</sup><sub>Al-Si</sub>=-3531+1.36T and L<sup>2</sup><sub>Al-Si</sub>= 2265 are the parameters of silicon in aluminum alloy[34], and L<sup>0</sup><sub>Al-Cu</sub>= -66622+8.1T, L<sup>1</sup><sub>Al-Cu</sub>=64800-90.8T+10T(Ln(T)) and L<sup>2</sup><sub>Al-Cu</sub>=-2812 are the parameters of copper in aluminum alloy [35]. According to the calculation from Eqs. (6) to (8), μ = 1.4 and 5.6 mPa are the viscosity of Al-12.6 wt%Si and Al-33 wt%Cu at their respective liquidus temperature. The other parameters were obtained from the default of the ANSYS software.

The surface tension (σ) was employed in the simulation. Eq. (9) [36] evaluates the surface tension (σ) as a function of temperature that starts from the liquidus temperature. In Eq. (9), σ=0.868 Nm<sup>-1</sup> for pure aluminum at melting temperature [26], σ<sub>L</sub> = 0.824 Nm<sup>-1</sup> and (dσ/dT) = (-3.1x10<sup>-4</sup>) Nm<sup>-1</sup> K<sup>-1</sup> for Al-12 wt%Si [37], σ<sub>L</sub>=0.951 Nm<sup>-1</sup> and (dσ/dT) = (-0.92x10<sup>-4</sup>) Nm<sup>-1</sup> K<sup>-1</sup> for Al-30 wt%Cu [36]. Fig. 2 (d) shows the comparison between the surface tension of Al-30 wt%Cu hypoeutectic alloy and Al-12 wt%Si hypoeutectic alloy, where both alloys lay near the eutectic alloy for Al-Cu and Al-Si systems.

$$\rho(T, C_{Si}) = A_L - B_L T$$

4

$$\rho(T, C_{Cu}) = 3150 + \beta_T(T - 549.8) + \beta_C(C_{Cu} - 33)$$

5

$$\ln(\eta_{Alloy}) = \sum_{i=1}^N x_i \ln(x_i \eta_i^0) + \left( \left\{ \sum_{i=1}^N x_i E_i + \Delta H_{sol} \right\} / R_o T \right)$$

6

$$\Delta H_{sol} = \Omega C_{Solute} C_{Al}$$

7

$$\Omega = \sum_{i=0}^j L^i (C_{Al} - C_{Solute})^i$$

8

$$\sigma(T) = \sigma_L + (d\sigma/dT)(T - T_L)$$

9

## 5 Results And Discussion

The experiments *Ex1* and *Ex2* involved in Table 1 were carried out by mixing *Alloy1* (pure aluminum) with *Alloy2* (eutectic alloy). The *Alloy1* and *Alloy2* were the precursor alloys placed in the phase diagram at points (A), (B), and (D) shown in Fig. 2 (a). The conditions of *Ex2* is almost similar to that of *Ex1* for *Alloy1*,  $m_1$ ,  $m_2$ ,  $T_1$ , and  $mr$ . Fig. 3 (a) to (d) show a comparison between the microstructure of the experiments *Ex1* and *Ex2*. Fig. 3 (a) and (b) show optical microstructure images of the CDS sample for the experiment denoted as *Ex1*. Fig. 3 (a) shows an optical microstructure image for the specimen located in the middle of the sample. The specimen is pointed by (A) in Fig. 1(f). In Fig. 3 (a) globular mixed with rosette morphologies would form the non-dendritic microstructure. Fig. 3 (b) shows an optical microstructure image for the specimen located at the edge of the sample. The specimen is pointed by (B) in Fig. 1(f). In Fig. 3 (b) dendritic morphologies mixed with rosette morphologies form the microstructure, where the dendrites dominate the microstructure. Fig. 3 (c) and (d) show optical microstructure images of the specimens located in the middle and the edge of the sample for the CDS experiment denoted as *Ex2*, respectively. In Fig. 3 (c) and (d), globular mixed with few rosette morphologies would form the non-dendritic microstructure. The microstructure results indicated in Fig. 3 (a) to (d) show that the undercooling employed from *Alloy2* for the Al-Cu system shown in Fig. 2 (a) strongly affects the non-dendritic microstructure leading to the creation of the globular morphologies that dominate the entire microstructure of the sample compared with that for the Al-Si system.

Figure 3 (e) shows the thermal curves of the experiments *Ex1* and *Ex2* drawn for the data collected by the lower thermocouple inserted in the crucible of *Alloy2* prior to the mixing step. In Figure 3 (e), the temperature data was superimposed to start at the same time to ease the comparison between the thermal curves, further, points (A) and (C) represent the starting of mixing of *Alloy1* into *Alloy2* and points (B) and (D) represent the maximum temperature of the mixture at the end of the mixing step for *Ex1* and *Ex2*, respectively. Figure 3 (e) also shows that thermal recalescence, some of them pointed by arrows, appear as an oscillation in the temperature happening between the starting and the end of mixing in the thermal curves for the experiments *Ex1* and *Ex2*, where this kind of thermal recalescence indicates that the nucleation events occur during the mixing step of the CDS process [12]. In addition, the difference between the starting of mixing temperatures (points (A) and (C)) was around  $582-552=30^\circ\text{C}$ , and the difference between the maximum temperatures (points (B) and (D)) was around  $657-650=7^\circ\text{C}$ . According to that, the nucleation can occur in both the Al-Si and Al-Cu systems, and the heat issued from the nucleation events during the mixing of pure aluminum into Al-33 wt%Cu is significantly bigger than that when mixing pure aluminum into Al-12.6 wt%Si although the conditions of *Ex2* is almost similar to that of *Ex1* for *Alloy1*,  $m_1$ ,  $m_2$ ,  $T_1$ , and  $mr$ .

Figure 4 (a) to (d) show the simulation results of density distribution at 0.4s for *Ex1* and *Ex2* experiments illustrated in Table 1. Figure 4 (a) to (c) show the simulation results of the density distribution for the *Ex1* experiment. Figure 4 (b) shows a magnified area at the funnel region shown in Figure 4 (a), showing that the liquid surface that was pointed by arrows forms as a curved shape happening because of the effect of the surface tension employed in the calculation. This appears in all liquid surfaces for Al-Si and Al-Cu

systems at all times in the present study when employing the surface tension in the simulation. Figure 4 (c) and (d) show magnified areas of the mixture in the crucible region for *Ex1* and *Ex2* respectively. The crucible region is pointed by the square in Figure 4 (a) taken as an example. In Figure 4 (c) and (d), the density distribution for *EX2* is significantly different compared with *Ex1*, wherein better distribution of *Alloy2* in the mixture for the Al-Cu system. Further, air bubbles that were pointed by arrows appear in both experiments forming at the contact area located between the stream of *Alloy1* and *Alloy2*. The simulation results show that the air bubbles forming in the Al-Cu system are significantly less than that for the Al-Si system shown in Figure 4 (d). One can suggest that the air bubbles forming during the mixing step strongly depend on the difference between the densities and the viscosities of the mixed alloys.

Figure 5 (a) to (f) show the simulation results of density distribution for the mixture in the crucible taken during the mixing step at 0.8s, 1.2s, and at the end of the mixing step for the experiments named *Ex1* and *Ex2* illustrated in Table 1. Where Figure 5 (a) and (b) show the density distribution after 0.8s, Figure 5 (c) and (d) show the density distribution after 1.2s, and Figure 5 (e) and (f) show the density distribution at the end of mixing for *Ex1* and *Ex2*, respectively. In Figure 5 (a) to (f), the eutectic alloy for the Al-Cu system has a better probability to break into small masses, this leads to making better distribution of *Alloy2* in the entire mixture. One can suggest that the better distribution of the two precursor alloys during the mixing step could affect forming a non-dendritic microstructure in the CDS process. Further, the simulation results show that the air bubbles distribute in the entire mixture by the agitation happening during the mixing, where some of them escape to the environment and the other exists in the mixture till the end of the mixing step.

Figure 6 (a) and (b) show typical microstructure images of the specimens located in the middle and the edge of the CDS sample for the experiment denoted as *Ex3* in Table 1, respectively. Figure 6 (a) shows an optical microstructure image for the specimen located in the middle of the sample, showing that the non-dendritic microstructure forms the middle of the CDS process sample. In Figure 6 (a) globular mixed with rosettes and a few dendritic morphologies would form the non-dendritic microstructure. Figure 6 (b) shows an optical microstructure image for the specimen located at the edge of the sample. In Figure 6 (b) the non-dendritic microstructure also has globular mixed with rosette and dendritic morphologies form in the edge of the sample. The microstructure of the experiment *Ex3* differs from that forming in *Ex1* especially at the edge of the sample. One can suggest that the experiment *Ex3* was carried out by increasing the mass of *Alloy1* (pure aluminum) and decreasing the mass of *Alloy2* (eutectic alloy), the nucleation starts from *Alloy1* (pure aluminum with 665°C) that is undercooled during the mixing because the mixing happens into the crucible of *Alloy2* that has a lower temperature (580°C) [16, 17]. Additionally, The decrease of *Alloy2* results in decreasing in the dendritic morphologies forming in the microstructure because the *Alloy2* is prone to make the dendritic microstructure, especially when choosing pure aluminum as *Alloy1* in the CDS process [17]. Further, the mixture was poured directly after mixing step into an empty crucible heated at 555°C. This leads to an increase in the nucleation rate in *Alloy1* and makes an agitation applying to the mixture leading to a re-distribution of the morphologies forming in the mixture. According to that, more agitation during and after the mixing step is preferred for the hypoeutectic Al-Si system[13]. Figure 6 (c) shows an optical microstructure image of a specimen taken

from the sample for the experiment named *Ex4* that was carried out by re-melting half the sample of the *Ex3* at 700°C and hence, the melt was directly poured into a hot empty backed- clay crucible heated at 555°C. The experiment *Ex4* represents the conventional solidification. In Figure 6 (c), the dendritic microstructure forms the entire sample. The microstructure results shown in Fig. 5 and Figure 6 would indicate that the Al-Si hypoeutectic alloys can form a non-dendritic microstructure via the CDS process when carefully choosing the  $mr$ ,  $T_1$ ,  $T_2$ , and the contents of the two precursor alloys.

Figure 7 (a) and (b) show typical microstructure images of the specimens located in the middle and the edge of the sample for the CDS experiment denoted as *Ex5* in Table 1, respectively. In Figure 7 (a) and (b) rosette mixed with equiaxed dendritic morphologies would form the microstructure. The microstructure of the experiment *Ex5* differs from that forming in *Ex1* and *Ex3*. The experiment *Ex5* was carried out to make the  $mr=3$  by decreasing the mass of *Alloy1* (pure aluminum) and increasing the *Alloy2* (eutectic alloy). The nucleation starts from *Alloy1* (pure aluminum with 665°C) that is undercooled during the mixing because the mixing happens into the crucible of *Alloy2* that has a lower temperature(580°C) [16, 17]. Additionally, The *Alloy2* was increased resulting in to increase in the dendritic microstructure because the *Alloy2* is prone to make the dendritic microstructure [17]. Further, the mixture was poured directly after mixing step into an empty steel crucible heated at 580°C. This leads to making an agitation to the mixture resulting in re-distributing of the morphologies forming in the entire mixture. Further, the stable solid-liquid interface that exists with the growing nuclei would break to become unstable because of the high cooling rate established between the mixture and the steel crucible that has higher thermal diffusivity compared with that for the backed-clay crucible used for *Ex1* to *Ex4* [12, 15]. Figure 7(c) shows an optical microstructure image taken from the sample for *Ex6* that was carried out by re-melting half of the sample for the *Ex5* at 700°C and hence, the melt was directly poured into the steel crucible heated at 580°C. In Figure 7 (c), the dendritic microstructure forms the entire sample. The columnar dendrites dominate the microstructure of the experiment *Ex6* because of the high cooling rate established between the mixture and the steel crucible.

Figure 8 shows an optical microstructure image of the CDS experiment denoted as *Ex7* in Table 1. In Fig. 8, a non-dendritic microstructure forms the entire sample for *Ex7*. The non- dendritic microstructure forms with lower dendrites compared with that for the CDS experiments *Ex1* to *Ex5*, although the mixing takes place at a lower mass ratio ( $mr=2.6$ ) and lower difference in the initial temperature (665-613= 42°C). This happens because the solidification of the *Alloy2* (Al-15wt%Si- hypereutectic alloy) differs from the solidification of hypoeutectic Al-Si alloys that are prone to form the dendritic microstructure. According to *Ex7* results and the results reported by Khalaf [38], a new window can be opened of the CDS process at which the two precursor alloys can be chosen as hypoeutectic alloy mixing with hypereutectic alloy to make the resultant alloy.

The CDS process was presented as a casting process depending on mixing two precursor alloys. Therefore, there are unlimited possibilities to choose the contents of the precursor alloys. The alloy Al-6.45Si-4Cu-0.5Mg-0.66Fe-0.66Zn was made by the CDS process in two different ways by choosing the *Alloy1* and *Alloy2* as illustrated in Table 2. Fig. 9 (a), (b), and (c) show typical microstructure images of

the specimens located in the middle and the edge of the sample for the CDS experiment denoted as *Ex8* and *Ex9* indicated in Table 2, respectively. Fig. 9 (a) shows a typical microstructure image of the specimen located in the middle of the CDS experiment denoted as *Ex8*. In Fig. 9 (a), the dendritic microstructure forms in the entire sample. Fig. 9 (b) and (c) show typical microstructure images of the specimens located in the middle and the edge of the sample for the CDS experiment denoted as *Ex9*. In Fig. 9 (b) and (c), the non-dendritic microstructure forms the entire sample, where, globular, rosette, and a few equiaxed dendritic morphologies would coexist in the microstructure. The significant result extracted from *Ex9* is that the non-dendritic microstructure forms in the entire sample although the difference between the temperatures of the precursor alloys was 11°C. The parameters illustrated in Table 2 of the experiment *Ex9* indicate that the *Alloy1* and *Alloy2* have 2 and 3°C superheat prior to the mixing step, respectively. Further, *Alloy2* has all the copper content and has the lower crucible temperature. One can suggest that lower superheat of *Alloy1* with less than 5°C and improving the spontaneous nucleation that may happen to make copious nucleation in the hypoeutectic Al-Si system [11, 16].

## 6 Conclusion

This study dedicates to changing the microstructure of the hypoeutectic Al-Si alloys from dendritic to non-dendritic microstructure by the controlled diffusion solidification process (CDS). Nine experiments representing the CDS process and conventional casting were carried out in this study. Pure aluminum and hypoeutectic alloys would be employed as the first precursor alloy while eutectic alloy for Al-Si system and Al-Cu system (used for comparison), hypoeutectic Al-Si alloys, and hypereutectic Al-Si alloys would be employed as the second precursor alloy (*Alloy2*), where *Alloy1* and *Alloy2* would be mixed with a mass ratios of 8.3, 6, 4.5, 3, and 2.6. The mixing of *Alloy1* into *Alloy2* happens directly and through a 9mm diameter funnel. The Al-Si and Al-Cu experiments that were mixed through the funnel were simulated by using Ansys fluent software to present a better understanding of the distribution of *Alloy2* in the mixture. The results of this study are summarized below:

1. The CDS process would change the microstructure of the hypoeutectic Al-Si alloys to a non-dendritic microstructure. The process presents many ways to choose the precursor alloys.
2. The non-dendritic microstructure forms the sample when pure aluminum with around 5°C superheat would be used as a first precursor alloy. In this case, increasing the mass ratio by decreasing the mass of *Alloy2* represents a solution to form the non-dendritic microstructure with lower dendrites forming in the CDS sample.
3. The simulation results carried out by Ansys software for the CDS process give a better explanation for the *Alloy1* and *Alloy2* distribution in the mixture during the mixing step.
4. The simulation results show that the air interrupted during the mixing step form between the *Alloy1* stream and *Alloy2* depending on the density and the viscosity of the mixed alloys.

5. The hypereutectic Al-Si alloys can be employed as *Alloy2* to form a non-dendritic microstructure for hypoeutectic Al-Si alloys. Where using the hypereutectic Al-Si alloys increases the mass ratio and changes the solidification pathway of *Alloy2* leading to reduce the dendrites forming during the solidification of the mixture.

6. The superheat of *Alloy1* and *Alloy2* less than 5°C is preferred to change the microstructure of hypoeutectic *alloys* when using alloys as *Alloy1*. This gives a better solution when the difference in temperature between the two precursor's alloys is less than 20°C for the alloys under study.

7. Pure aluminum employed as *Alloy1* needs more undercooling to form the non-dendritic microstructure compared with employing an alloy.

The variation in choosing the precursor alloys in this study explains the parameters preferred to form the non-dendritic microstructure in hypoeutectic Al-Si alloys.

## Abbreviations

<i>Alloy1</i>	First precursor alloy	$T$	Temperature (K)
<i>Alloy2</i>	Second precursor alloy	$T_1$	<i>Alloy1</i> Temperature (K)
<i>Alloy3</i>	Resultant alloy.	$T_2$	<i>Alloy2</i> Temperature (K)
$A_L$ and $B_L$	Variables of density	$T_L$	Liquidus temperature (K)
$C_1$	Composition of <i>Alloy1</i> (wt %)	$T_S$	Liquidus temperature (K)
$C_2$	Composition of <i>Alloy2</i> (wt %)	$T_{L1}$	liquidus temperature of <i>Alloy1</i> (K)
$C_{Al}$	Aluminum concentration (wt%)	$T_{L2}$	liquidus temperature of <i>Alloy2</i> (K)
$C_{Cu}$	Copper concentration (wt%)	$T_\infty$	Bulk temperature (K)
$C_o$	Composition of <i>Alloy3</i> (wt %)	$U$	Velocity ( $\text{ms}^{-1}$ )
$C_P$	Specific heat ( $\text{Jkg}^{-1}\text{K}^{-1}$ )	$\beta_T$	temperature dependence Variable
$C_{Si}$	Silicon concentration (wt%)	$\beta_C$	concentration dependence Variable
$C_{Solute}$	Solute concentration (wt%)	$\mu$	Viscosity (mPa)
$H_{sol}$	Heat of solution (J)	$\Omega$	Regular solution
$m1$	Mass of <i>Alloy1</i> (kg)	$K$	Thermal conductivity ( $\text{WK}^{-1}\text{m}^{-2}$ )
$m2$	Mass of <i>Alloy2</i> (kg)	$\sigma$	Surface tension ( $\text{Nm}^{-1}$ )
$mr$	Mass ratio ( $m_1/m_2$ )	$\rho$	Density ( $\text{kgm}^{-3}$ )
$N$	Number of species	$\eta_{Alloy}$	Multy component viscosity ( mPa)

## Declarations

### Acknowledgment

The authors are grateful to Mr. Doug Culley, Mr. Xiaogang Li, and Xiaochun Zheng for assisting in this research project.

### Author contribution

Abbas A. Khalaf designed the study, performed the research, analyzed the data, wrote the paper, conducted experiments and data processing.

### Funding

The authors declare that no funds, grants, or other support were received during the preparation of this manuscript.

### **Availability of data and materials**

The experimental and simulation data is transparent.

### **Ethics approval**

This article does not contain any studies with human participants performed by any of the authors.

### **Consent to participate**

This work was conducted with no human test subjects.

### **Consent for publication**

This work has consent for publication

### **Conflict of interest**

The authors declare that they have no conflict of interest.

## **References**

1. Ye H (2003) An Overview of the Development of Al-Si-Alloy Based Material for Engine Applications. *J Mater Eng Perform* 12:288–297. <https://doi.org/10.1361/105994903770343132>
2. Ahn SS, Pathan S, Koo JM et al (2018) Enhancement of the mechanical properties in Al-Si-Cu-Fe-Mg alloys with various processing parameters. *Materials (Basel)* 11. <https://doi.org/10.3390/ma11112150>
3. Timpel M, Wanderka N, Schlesiger R et al (2012) The role of strontium in modifying aluminium-silicon alloys. *Acta Mater* 60:3920–3928. <https://doi.org/10.1016/j.actamat.2012.03.031>
4. Mirzadeh H, Niroumand B (2009) Fluidity of Al-Si semisolid slurries during rheocasting by a novel process. *J Mater Process Technol* 209:4977–4982. <https://doi.org/10.1016/j.jmatprotec.2009.01.020>
5. Saha D, Shankar S, Apelian D, Makhlof MM (2004) Casting of aluminum-based wrought alloys using controlled diffusion solidification. *Metall Mater Trans A* 35:2174–2180. <https://doi.org/10.1007/s11661-004-0167-8>
6. Khalaf AA, Ashtari P, Shankar S (2009) Controlled Diffusion Solidification (CDS): Conditions for Non-Dendritic Primary Aluminum Phase in Al-Cu Hypo-Eutectic Alloys. In: *The Third International Symposium, TMS (The Minerals, Metals & Materials Society)*. pp 215–222

7. Saha D, Shankar S, Apelian D, Makhoul MM (2005) Controlled diffusion solidification- Manufacturing net shaped Al-based wrought alloy parts. In: Proceedings of the John Campbell Honorary Symposium Edited by P. Crepeau and M. Tiryakioglu TMS (The Minerals, Metals & Materials Society)
8. Ashtari P, Birsan G, Khalaf A et al (2011) Controlled diffusion solidification of 2024,6082 and 7075 Al alloys via tilt-pour casting process. *Int J Met* 5:43–63
9. Ghiaasiaan R, Zeng X, Shankar S (2014) Controlled Diffusion Solidification (CDS) of Al-Zn-Mg-Cu (7050): Microstructure, heat treatment and mechanical properties. *Mater Sci Eng A* 594:260–277
10. Khalaf AA, Shankar S (2011) Favorable environment for a nondendritic morphology in controlled diffusion solidification. *Metall Mater Trans A* 42:2456–2465
11. Khalaf AA (2010) Controlled diffusion solidification: process mechanism and parameter study. Ph.D Thesis. McMaster University
12. Khalaf AA, Shankar S (2020) Mechanism of Anomalous Grain Formation During Controlled Diffusion Solidification. <https://doi.org/10.1007/s11837-020-04198-1>. JOM
13. Khalaf AA, Shankar S (2012) Effect of mixing rate on the morphology of primary Al phase in the controlled diffusion solidification (CDS) process. *J Mater Sci* 47:8153–8166
14. Khalaf AA, Ashtari P, Shankar S (2009) Formation of nondendritic primary aluminum phase in hypoeutectic alloys in controlled diffusion solidification (CDS): A hypothesis. *Metall Mater Trans B* 40:843–849
15. Khalaf AA (2016) Mechanism of controlled diffusion solidification: Mixing, nucleation and growth. *Acta Mater* 103:301–310
16. Khalaf AA, Takrouri KJ (2020) Spontaneous nucleation in hypoeutectic Al – Cu system by controlled diffusion solidification process. *SN Appl Sci* 2:1337
17. Khalaf AA (2021) Studying of Non-Dendritic Microstructure Forming in Controlled Diffusion Solidification. *Int J Met*. <https://doi.org/10.1007/s40962-021-00590-y>
18. Ghiaasiaan R, Shankar S (2020) Microstructure, Intermetallic Phases, and Fractography of the Cast Al-5.8Zn-2.2Mg-2.5Cu Alloy by Controlled Diffusion Solidification. *Metall Mater Trans A Phys Metall Mater Sci* 51:4711–4726. <https://doi.org/10.1007/s11661-020-05885-z>
19. Ghiaasiaan SR, Khalaf AA, Zheng X, Shankar S (2012) Near net shaped casting of 7050 Al wrought alloy by CDS process: Microstructure and mechanical properties. In: *Light Metals 2012*. pp 313–318
20. Ghiaasiaan SR, Shankar S, Apelian D (2014) Control Diffusion Solidification (CDS): An Overview of Mechanism and Application. *Shape Cast 5th Int Symp 2014* 89–97. <https://doi.org/10.1002/9781118888100.ch11>
21. Ghiaasiaan SR, Khalaf AA, Zheng X, Shankar S (2012) Near Net Shaped Casting of 7050 Al Wrought Alloy By CDS Process: Microstructure and Mechanical Properties. In: TMS (The Minerals, Metals & Materials Society). pp 313–318

22. Ghiaasiaan SR (2015) Controlled diffusion solidification process (CDS) of Al-7XXX wrought alloys: heat treatment, microstructure, and mechanical properties. McMaster University
23. Yang X, Li Y, Luo X, mei et al (2019) Microstructural evaluation and mechanical properties of 7075 aluminum alloy prepared by controlled diffusion solidification. *China Foundry* 16:238–247. <https://doi.org/10.1007/s41230-019-9059-9>
24. Pourgharibshahi M, Divandari M, Saghafian Larijani H, Ashtari P (2017) Controlled diffusion solidification processing: A review. *J Mater Process Technol* 250:203–219. <https://doi.org/10.1016/j.jmatprotec.2017.07.018>
25. Symeonidis K (2009) The controlled diffusion solidification process: fundamentals and principles. Ph.D Thesis. Worcester Polytechnic Institute (WPI)
26. Apelian D, Makhlof MM, Saha D (2006) CDS Method for Casting Aluminium-Based Wrought Alloy Compositions: Theoretical Framework. In: *Materials Science Forum*. pp 1771–1776
27. Ashtari P, Birsan G, Khalaf A, Shankar S (2011) Controlled diffusion solidification of 2024,6082 and 7075 Al alloys via tilt-pour casting process. *Int J Met* 43–63
28. Wu M, Ludwig A (2009) Modeling equiaxed solidification with melt convection and grain sedimentation-II. Model verification. *Acta Mater* 57:5632–5644. <https://doi.org/10.1016/j.actamat.2009.07.067>
29. Valencia JJ, Quedstedt PN (2008) ASM Handbook Committee/Thermophysical Properties
30. Kurz W, Fisher DJ (1984) *Fundamentals of Solidification*, Second Edition. Trans Tech Publications, Aedermannsdorf
31. Dogan A, Arslan H (2018) Thermophysical properties of Cu–In–Sn liquid Pb-free alloys: viscosity and surface tension. *Philos Mag* 98:37–53. <https://doi.org/10.1080/14786435.2017.1392053>
32. Zhang F, Du Y, Liu S, Jie W (2015) Modeling of the viscosity in the AL-Cu-Mg-Si system: Database construction. *Calphad Comput Coupling Phase Diagrams Thermochem* 49:79–86. <https://doi.org/10.1016/j.calphad.2015.04.001>
33. Yoshikawa T, Morita K (2006) Activity measurements of Al and Cu in Si – Al – Cu melt at 1273 and 1373 K by the equilibration with molten Pb. *J Alloys Compd* 420:136–144. <https://doi.org/10.1016/j.jallcom.2005.10.071>
34. Miettinen J et al (2019) Thermodynamic Description of the Fe-Al-Mn-Si- C System for Modelling Solidification of Steels
35. Wang F, Liu ZL, Qiu D et al (2015) The Influence of the Effect of Solute on the Thermodynamic Driving Force on Grain Refinement of Al Alloys. *Metall Mater Trans A Phys Metall Mater Sci* 46:505–515. <https://doi.org/10.1007/s11661-014-2599-0>
36. Schmitz J, Brillo J, Egry I, Schmid-Fetzer R (2009) Surface tension of liquid Al-Cu binary alloys. *Int J Mater Res* 100:1529–1535. <https://doi.org/10.3139/146.110221>
37. Kobatake H, Brillo J, Schmitz J, Pichon PY (2015) Surface tension of binary Al–Si liquid alloys. *J Mater Sci* 50:3351–3360

## Figures

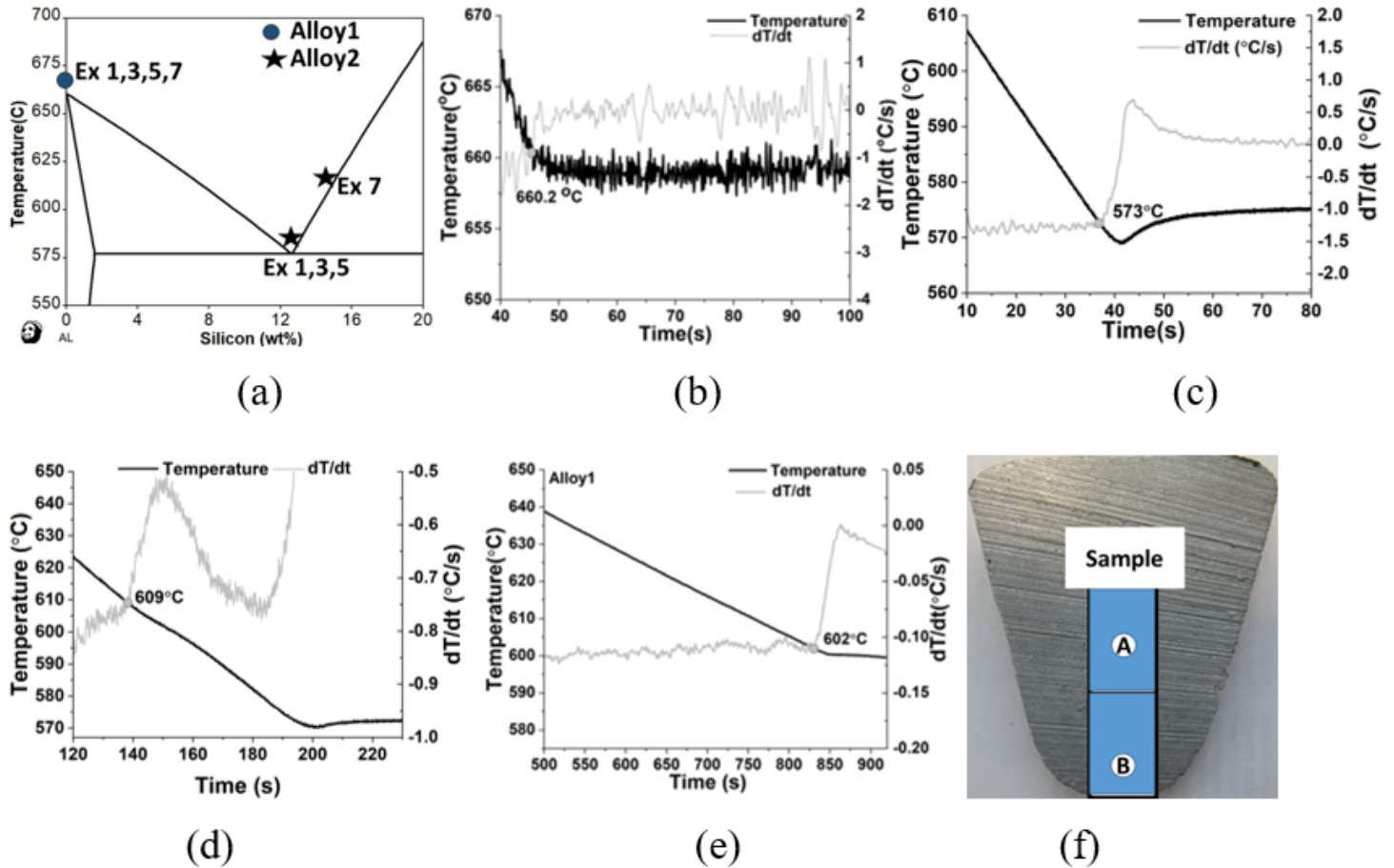


Figure 1

(a) Al-Si phase diagram showing the location of *Alloy1* and *Alloy2* prior to mixing step, (b), (c), and (d) cooling curve and first derivative curve for pure aluminum, Al-12.6 wt%Si, and Al-15 wt%Si, respectively, (e) cooling curve and first derivative curve for the *Alloy1* for *Ex9* involved in Table 2, and (f) half of solidified sample of the experiments showing the locations of the middle and the edge specimens taken for the microstructure image.

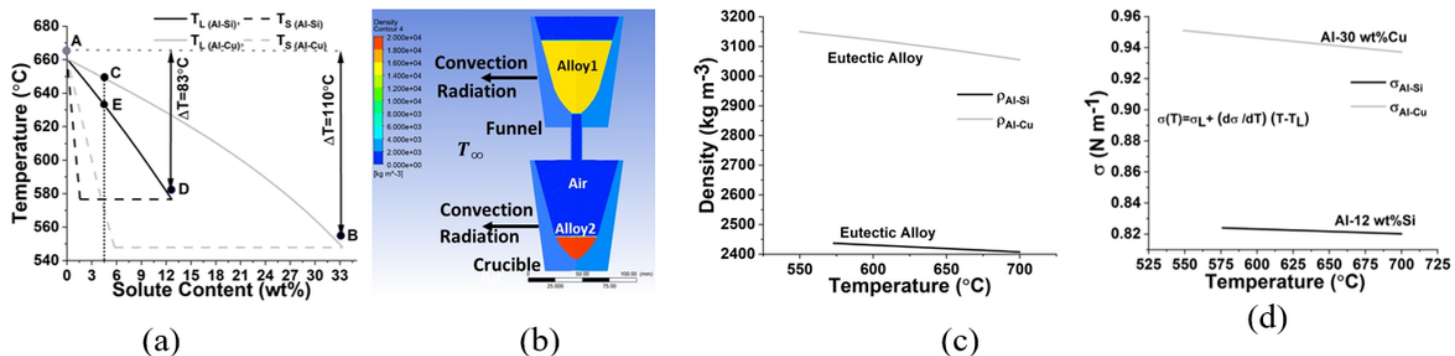


Figure 2

(a) Al-Si and Al-Cu phase diagram for hypoeutectic area showing the liquidus and solidus lines, (b) initial condition of the density for air, Alloy1 and Alloy2 coexisting in the model solved by ANSYS software (c) comparison between the density of Al-12.6 wt%Si and Al-33 wt%Cu, and (d) comparison between the surface tension of Al- 12 wt%Si and Al-30 wt%Cu.



Figure 3

Typical microstructure images of the sample for the CDS experiments named Ex1 and Ex2 involved in Table 1, (a) middle specimen for Ex1, (b) edge specimen for Ex1, (c) middle specimen for Ex2, (d) edge specimen for Ex2, and (e) (a) thermal curves of the experiment named Ex1 and Ex2 shown in Table 1.

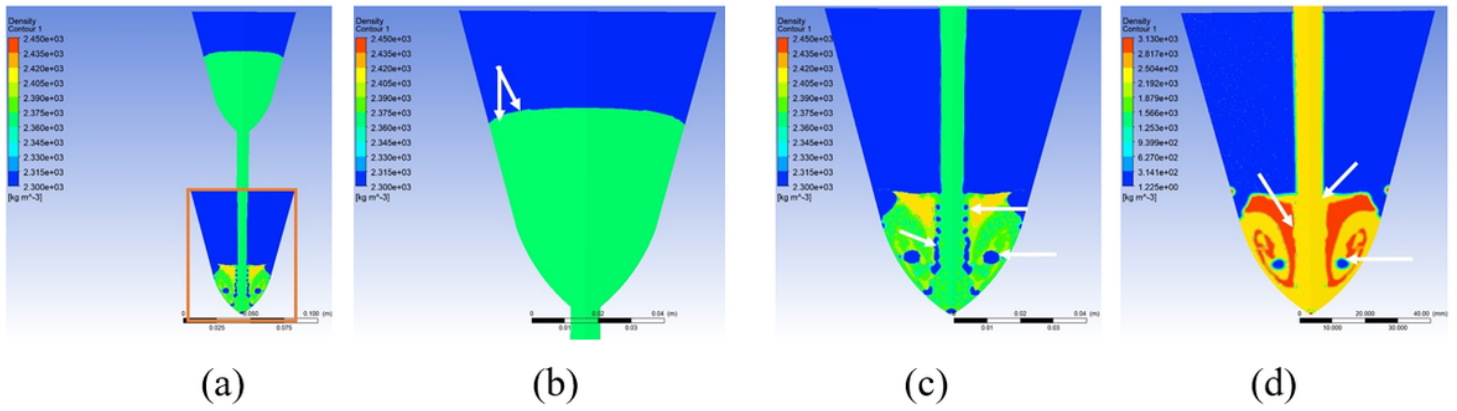


**Figure 4**

(a) density distribution at 0.4s of *Ex1* experiment for Al-Si system, (b) magnified image at funnel area shown in Fig 4(a), (c) magnified image at the crucible area pointed by a square shown in Fig 4(a) for *Ex1*, (d) magnified image of density distribution result at 0.4s for the crucible area of *Ex2* experiment for Al-Cu system.

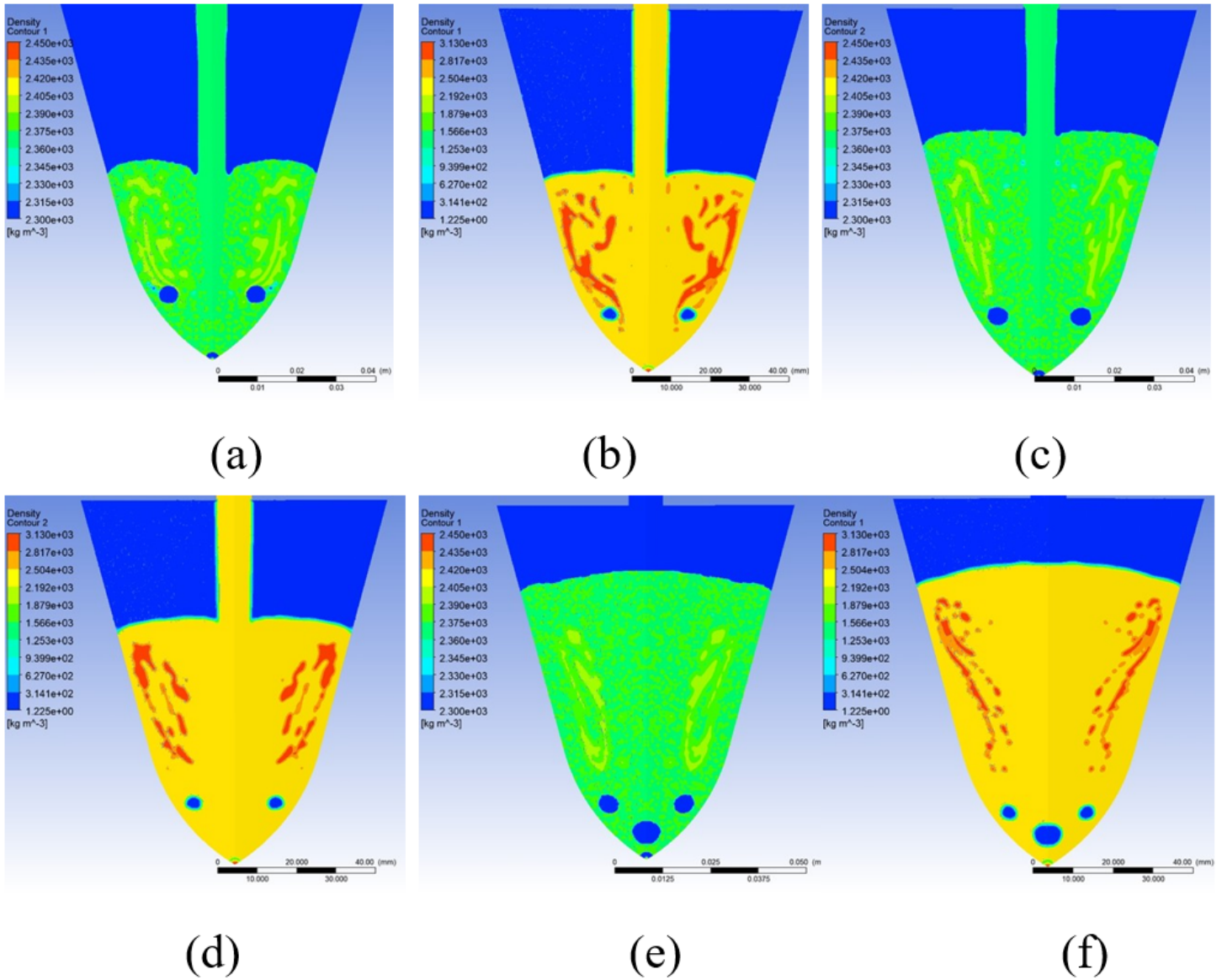


**Figure 5**

Simulation results of density distribution for *Ex1* and *Ex2* experiments, (a) and (b) taken at 0.8s, (c) and (d) taken at 1.2s, (e) and (f) taken at the end of mixing, respectively.

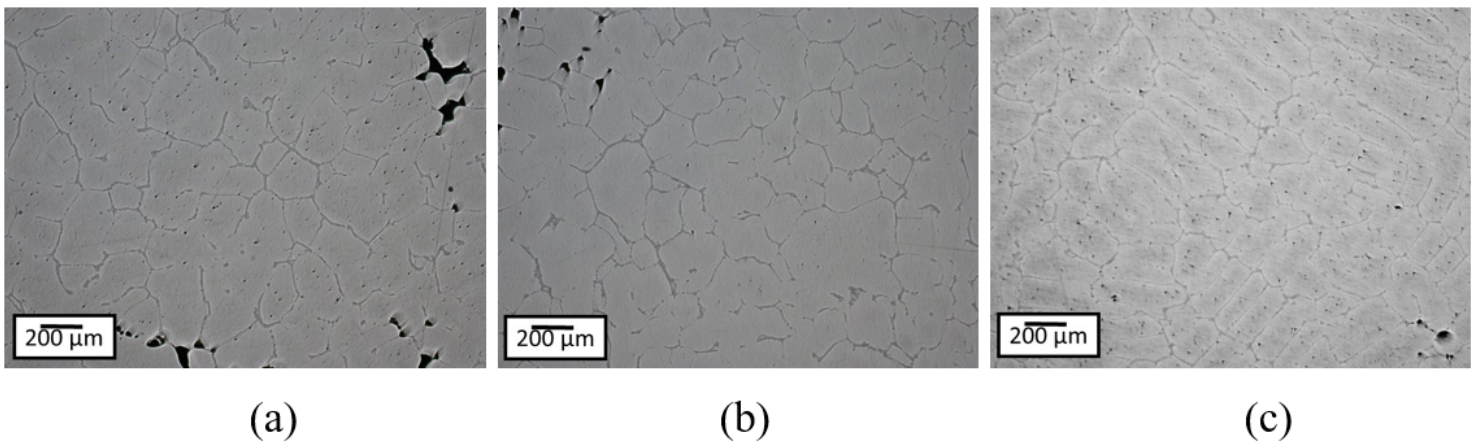


## Figure 6

(a) optical microstructure image taking from the middle of the sample for the experiment named *Ex3* shown in Table 1, (b) optical microstructure image taking from the edge of the sample for the experiment named *Ex3* in Table 1 and (c) optical microstructure image taking from the middle of the sample for the experiment named *Ex4* in Table 1.

## Figure 7

(a) optical microstructure image taking from the middle of the sample for the experiment named *Ex5* in Table 1, (b) optical microstructure image taking from the edge of the sample for the experiment named *Ex5* in Table 1 and (c) typical microstructure image taking from the middle of the sample for the experiment named *Ex6* in Table 1.

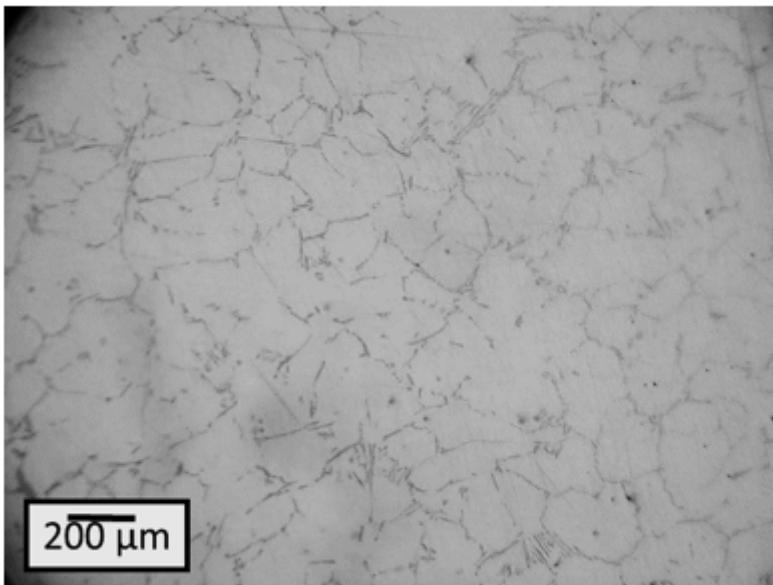


## Figure 8

typical microstructure image of the sample for the experiment named *Ex7* involved in Table 1



## Figure 9

(a) optical microstructure image taken from the middle of the sample for the experiment named *Ex8* in Table 2, (b) optical microstructure image taken from the middle of the sample for the experiment named *Ex9* in Table 2, and (c) optical microstructure image taken from the edge of the sample for the experiment named *Ex9*.

## Supplementary Files

This is a list of supplementary files associated with this preprint. Click to download.

- [GraphicalAbstract.jpg](#)